




Distortion-free amplification of 100 GHz mode-locked optical frequency comb using quantum dot technology

VICTORIA CAO,^{1,†}  SHUJIE PAN,^{1,†} YULONG FAN,² DINGYI WU,² MINGCHU TANG,¹ ALWYN SEEDS,¹ HUIYUN LIU,¹ XI XIAO,² AND SIMING CHEN^{1,3,4,*}

¹Department of Electronic and Electrical Engineering, University College London, Torrington Place, London WC1E 7JE, UK

²National Information Optoelectronics Innovation Center, China Information and Communication Technologies Group Corporation (CICT), Wuhan 430074, China

³Key Laboratory of Semiconductor Materials Science, Institute of Semiconductors, Chinese Academy of Sciences, Beijing 100083, China

⁴College of Materials Science and Opto-Electronic Technology, University of Chinese Academy of Science, Beijing 101804, China

[†]These authors contributed equally to this work.

*smchen@semi.ac.cn

Abstract: Semiconductor mode-locked optical frequency comb (ML-OFC) sources with extremely high repetition rates are central to many high-frequency applications, such as dense wavelength-division multiplexing. Dealing with distortion-free amplification of ultra-fast pulse trains from such ML-OFC sources in high-speed data transmission networks requires the deployment of semiconductor optical amplifiers (SOAs) with ultrafast gain recovery dynamics. Quantum dot (QD) technology now lies at the heart of many photonic devices/systems owing to their unique properties at the O-band, including low alpha factor, broad gain spectrum, ultrafast gain dynamics, and pattern-effect free amplification. In this work, we report on ultrafast and pattern-free amplification of ~100 GHz pulsed trains from a passively ML-OFC and up to 80 Gbaud/s non-return-to-zero (NRZ) data transmission using an SOA. Most significantly, both key photonic devices presented in this work are fabricated from identical InAs/GaAs QD materials operating at O-band, which paves the way for future advanced photonic chips, where ML-OFCs could be monolithically integrated with SOAs and other photonic components, all originated from the same QD-based epi-wafer.

Published by Optica Publishing Group under the terms of the [Creative Commons Attribution 4.0 License](https://creativecommons.org/licenses/by/4.0/). Further distribution of this work must maintain attribution to the author(s) and the published article's title, journal citation, and DOI.

1. Introduction

The advanced optical frequency comb (OFC) technology has profoundly impacted not only the optical communication system but also blossoming in other research fields, such as spectroscopy, metrology, frequency synthesis, attosecond science, and astrophysics [1–9]. While OFC characteristics can be realised via various photonic integrated circuit (PIC) strategies, semiconductor laser leveraging mode-locked (ML) techniques reap the benefits of being a compact, low-cost fabrication, and highly efficient operation and have emerged as a critical component for fibre-optic communication networks [10–13]. Fully harnessing the evenly spaced discrete frequency lines generated by the ML-OFC facilitates the voluminous parallelisation in dense wavelength division multiplexing (DWDM) transceivers, thereby embracing the challenges for the ever-growing global internet traffic caused by explosive digital activities [14,15].

While underlining the importance of high bandwidth density and spectral efficiency, the operating telecommunications window must also be considered to resolve the bandwidth limitation. Although the fully exploited C-band (1530 nm-1565 nm) remains the workhorse in long-haul transmission, O-band (1260 nm-1360 nm) with broader bandwidth and zero dispersion property becomes more attractive for short-reach communication links, as in data centres, metro, and access networks. Leveraging the ML-based comb source in O-band, which serves as a multi-channel optical carrier in the DWDM system, is of great appeal to expand data transmission capacity and information processing capabilities.

In high-capacity communication networks, as network traffic increases, the frequency spacings of ML-OFC sources must be increased. For example, 100 GHz frequency spacing operation is a vital target for beyond 400 Gb ethernet applications [16]. Apart from semiconductor lasers generating high-repetition-rate optical pulses, semiconductor optical amplifiers (SOAs) are also of considerable interest in tele- and data communications owing to their compact size, high gain, and optoelectronic compatibility, and play a crucial role in alleviating the power requirement of the light source, as well as compensating for the losses in the communication links [17–20]. However, dealing with distortion-free amplification of ultrashort optical pulses at high frequency spacings in high-speed data transmission networks requires such SOAs with ultrafast carrier dynamics.

Quantum dot (QD) technology continues to be at the centre of the quest for many photonic devices due to their unique properties at the O-band, such as low threshold [21,22], low alpha factor [23,24], greater resilience to temperature [25,26], and reduced amplified spontaneous emission efficiency [27]. With the additional features of insensitivity to defects and optical feedback, QD materials have become suitable candidates for the next generation of III-V on silicon telecommunication lasers [28–31]. Moreover, in the context of ultrafast science and technology, QD materials, which demonstrate broad gain bandwidth and ultra-fast carrier dynamics, have become one of the most promising materials systems for the generation and amplification of ultrashort optical pulses at a high frequency spacing [18,32].

As a result, impressively, these advanced properties of QD structure have enabled ML-OFC to exhibit compelling performance at O-band, including an ultra-high fundamental repetition rate of 100 GHz without imposing a Harmonic mode-locking technique [33], pulse width down to 390 fs without pulse compression [34], a record-high flat-top 3 dB bandwidth of 11.5 nm [11], an extremely stable operation to a record temperature of 120°C [12], a very low timing jitter below 7.5 fs [35] and so on. Notably, on the other hand, it was also demonstrated that QD-SOA could amplify sub-200-fs short pulses [36], and pulse with repetition rates of up to 80 GHz [37].

In this work, we aim to develop a cost-effective, advanced QD echo system where vital photonic devices are to be developed based on QD technology to generate and amplify ultrashort optical pulses at high frequency spacings for high-speed data transmission. In this context, we simultaneously fabricate ML-OFCs and SOAs originating from the identical InAs QD epi-wafer and demonstrate distortion-free amplification at frequency spacings of up to 100 GHz with pulse widths down to 1.8 ps and up to 80 Gbaud/s non-return-to-zero (NRZ) data transmission. Importantly, investigations into dynamic characterisations of amplified QD ML-OFC at high-speed links imply that the QD SOA exhibits enhanced eye diagram and lower bit error rate (BER) compared with a commercial praseodymium-doped fibre amplifier (PDFA) and thus brings enormous cost and size advantages. Interestingly, it is observed that the QD SOA does not affect the pulse width after the amplification of optical comb lines. Instead, it helps suppress the relative intensity noise (RIN) level at low frequencies, which is significant for high-speed communication applications. All these results provide valuable insight into the forefront QD-based monolithically integrated photonic chips and reveal an economical, compact, low-noise solution for short-reach DWDM optical sources.

2. Material growth and device structure

In this work, an InAs/GaAs QD laser structure, as seen in Fig. 1(a), was grown on a Si-doped GaAs (001) substrate using molecular beam epitaxy (MBE). The epitaxy starts with a 300 nm thick n-type GaAs buffer layer followed by a combination of silicon n-type doped $\text{Al}_x\text{Ga}_{1-x}\text{As}$ in a thickness of 1440 nm, which acts as the lower cladding layer. Above the lower cladding layer is the active region, consisting of a tenfold layer stack of InAs QDs sandwiched between two unintentionally doped GaAs waveguides. Then, a 1440 nm beryllium p-type doped $\text{Al}_x\text{Ga}_{1-x}\text{As}$ graded-index upper cladding layer was formed, and finally, a 400 nm highly p-type doped GaAs contact layer.

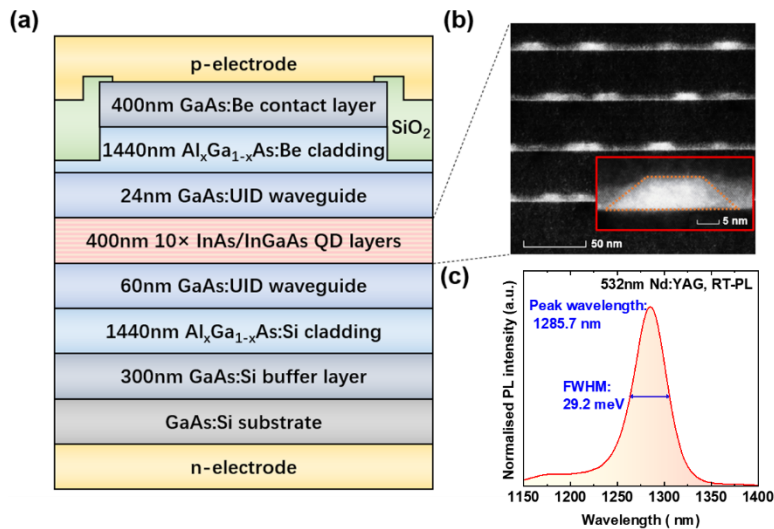


Fig. 1. Epitaxial structure and material property. (a) Schematic showing the layer structure of the QD ridge-waveguide devices. (b) Cross-sectional TEM image showing part of the QD active layers with a zoom-in view of the high-resolution single QD. (c) RT PL spectrum of the wafer sample.

To achieve high repetition rates in ML-OFC and to increase input power level without saturation in SOA, it is vital to enhance the optical gain of such devices. Here, this was achieved by depositing a more giant (10-layer stacks) than a usual number (5-8 layer stacks) of QD layers, with higher dot area density for each layer. In doing so, for the growth of the QD active region, instead of using a conventional InAs/InGaAs/GaAs dot-in-a-well (DWELL) structure, where the InAs layer is sandwiched by InGaAs layers. Here, each InAs QD layer stack was formed by depositing a three-monolayer InAs QD layer directly on the GaAs layer, with a V/III ratio of 30 and nucleation temperature of 500 °C. The growth rate of InAs QDs is 0.1 ML/s. As a result, a high dot area density of $6 \times 10^{10} \text{ cm}^{-2}$ was achieved, nearly doubling our previous result in terms of dot density [30]. The InAs QDs were then covered by a 3.7 nm $\text{In}_{18}\text{Ga}_{82}\text{As}$ strain-reducing layer, and such coverage growth conditions were also optimised to suppress atom migration during the coverage. By doing so, the original uniformity can be maintained without sacrificing dot density and multilayer structures. All these efforts led to a high gain achieved in this work.

Cross-sectional scanning transmission electron microscopy (TEM) measurements were used to characterize the QD active region. The typical dot size is ~ 20 nm in diameter and ~ 7 nm in height, as shown in Fig. 2(b). The high-resolution high-angle annular dark-field scanning TEM images of a single dot also, to a large extent, shows a uniform indium distribution with marginal intermixing, as shown in the inset of Fig. 2(b). A strong room-temperature (RT)

photoluminescence (PL) emission at ~ 1285 nm, originating from the ground state (GS) of QDs, with a full-width at half-maximum (FWHM) of 29.2 meV was obtained, as shown in Fig. 2(c). Another small emission peak at around 1180 nm contributed to the first excited state (ES1) transition was also identified in the PL spectrum. The existence of this ES1 acts as a carrier reservoir for the GS and plays a crucial role in the fast carrier dynamics and gain recovery of the QD structure [38].

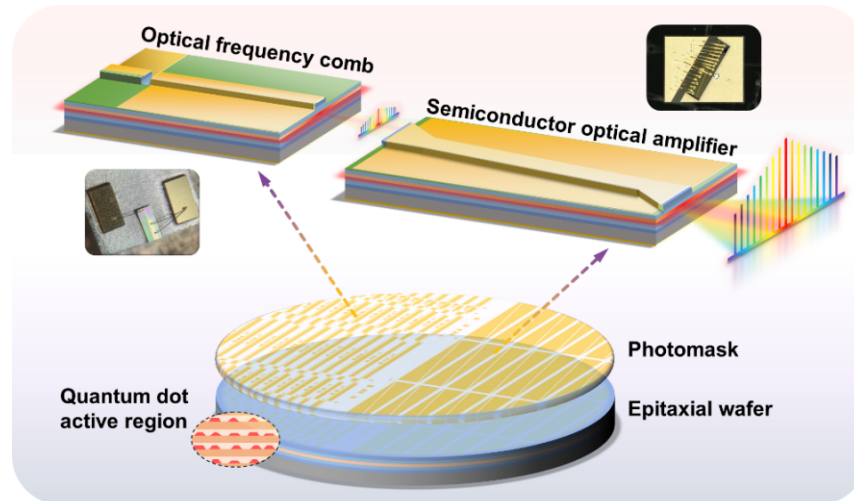


Fig. 2. Schematic drawing of ML-OFC source and SOA structures fabricated from the same QD wafer, including photographs of the top-view of the ML-OFC chip and SOA chip before packaging.

As illustrated in Fig. 2, both ML-OFCs and SOAs were fabricated simultaneously from the same QD epi-wafer described above following standard photolithography, etching and metal-dielectric deposition techniques. For the passively ML-OFC source, the ridge width is fixed at $5\ \mu\text{m}$. For achieving ~ 100 GHz fundamental repetition rates, the total length of the cavity was set to be $400\ \mu\text{m}$ with the length of the absorber designed to be $56\ \mu\text{m}$, corresponding to a gain-to-absorber length ratio of $\sim 6:1$. The rear facet of the ML-OFC was coated with a 95% high-reflection (HR) coating, and the light output from the gain section was left as-cleaved. For the travelling-wave SOA, the total gain section length is $1800\ \mu\text{m}$. The ridge width was designed to be $2\ \mu\text{m}$ at the centre of the gain section and increased linearly to $4\ \mu\text{m}$ towards both facets. Each tapered region has a length of $150\ \mu\text{m}$. The utilisation of this tapered design facilitates higher saturation output power (SOP) by effectively increasing the cross-sectional area of the QD active region [39]. Using this approach combined with the use of an 8° tilted waveguide angle with respect to the facet helps to suppress residual reflection and avoid lasing. Antireflection (AR) coating was applied to both as-cleaved facets of the SOA bar to further minimise the facet reflectivity to $< 0.3\%$. The selected individual chips were then indium-pasted on the sub-mount and gold-wire-bonded. The sub-mount for the SOA was specially designed with a tilted angle of 31° according to Snell's law (See the photograph in Fig. 2). In this way, the light emitted from the chip can be easily coupled into the fibre. Further minimisation in the coupling loss of the chip-fibre interface was done by utilising an AR-coated tapered lensed single-mode fibre (SMF). Finally, both chip-on-sub-mounts were Butterfly packaged with a standard Peltier cooler and a thermistor to enable testing. No optical isolators were used in the measurement setup or the butterfly packages. Unless stated otherwise, all measurements were carried out at room temperature (RT) under continuous-wave (CW) operation.

3. Characterisation and discussion

3.1. Ultra-fast repetition rate ML-OFC source

It is worth mentioning that, for the passively mode-locked QD two-section laser presented in this work, a stable mode-locking phenomenon was obtained without applying a reverse bias to the saturation absorber (SA) section, indicating that the SA can be recovered fast enough to its initial state of high loss even without the help of reverse bias attributed to an ultrafast recovery time of QDs. Thus, the SA section was left floating for the following experiments. Figure 3(a) shows the RT CW L-I characteristics of the passively mode-locked QD two-section laser with the SA section unbiased. The obtained threshold current is 18 mA, and the slope efficiency is 0.09 W/A. The measured output power coupled into a SMF is 5.5 mW at a driving current of 80 mA. It should be mentioned that the actual power from the device is higher than this recorded power value as there exists a coupling loss between the device facet and the fibre end, and the estimated coupling loss is 2.8 dB in this case. Optimizing the front facet reflectivity is expected to reduce the threshold current and increase external quantum efficiency. The mode-spacing of adjacent tones, i.e., the repetition rate of the device, is evaluated through a high-resolution optical spectrum analyser (OSA) (APEX AP2087A). The optical spectrum of four tones located near the central wavelength of 1291 nm at 66 mA is shown in Fig. 3(b). A mode-spacing of 0.523 nm is obtained, corresponding to a fundamental repetition rate of 96 GHz. To the best of our knowledge, this represents the highest repetition rate generated directly from a passively mode-locked QD two-section OFC at O-band.

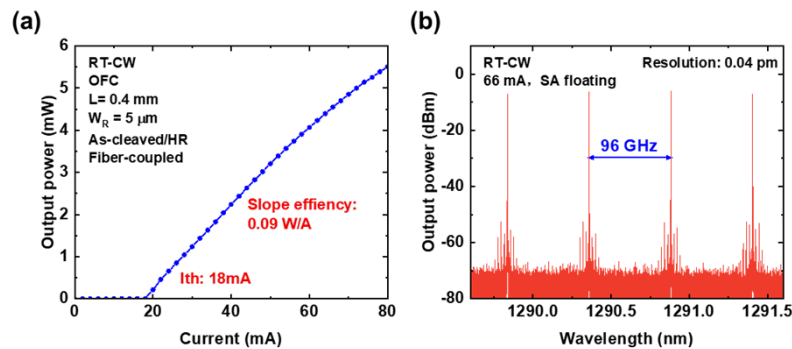


Fig. 3. QD ML-OFC RT static characteristics with no voltage bias. (a) CW L-I curve of the device. (b) Lasing spectrum showing adjacent channels measured at 66 mA current. (Resolution:0.04 pm)

3.2. High gain SOA static characteristics

Figure 4(a) shows in-fibre amplified spontaneous emission (ASE) power measured from both facets as a function of the current. As seen, above a current of ~ 50 mA, an apparent superluminescent behaviour is evidenced by the super-linear increase in output power with increasing current, indicating that the device is operating as an SOA. Power saturation is observed at high injections mainly due to the self-heating effect of the device. The discrepancy in output ASE power from each facet is primarily due to the different coupling losses and non-uniformity of facet coating caused by manufacturing fluctuations. In this work, the coupling loss was determined during the fibre alignment process at a current of 100 mA with respect to the power measured directly from the integrating sphere. The total coupling loss is 2.7 dB for facet A and 4.2 dB for facet B, including the loss between the chip-fibre interface, as well as the 0.15 dB propagation loss within the SMF. It is worth mentioning that the actual coupling loss should be larger than

the reported value since there was a gap between the chip and the integrating sphere due to the tailor-made sub-mount with a tilted angle for measurement before fibre coupling. For the following experiments, we use facet A as the input port and facet B with more significant coupling loss as the output port of the SOA.

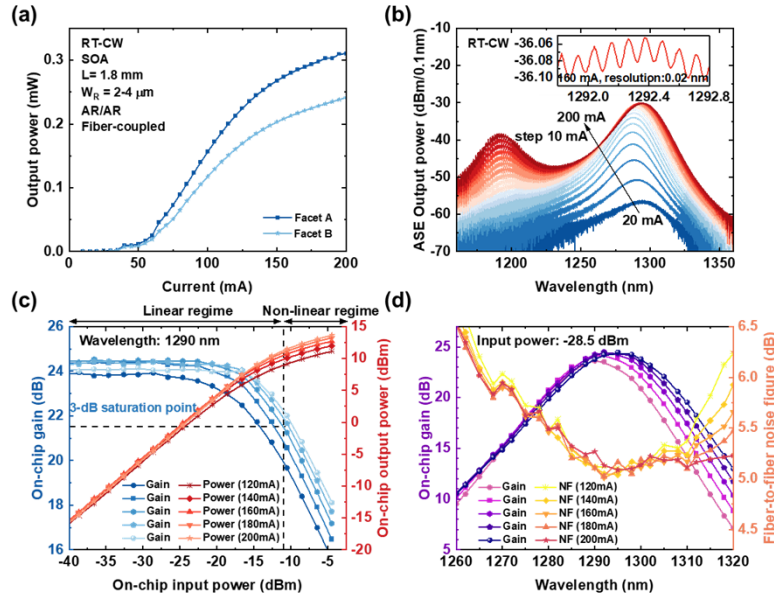


Fig. 4. QD SOA RT static characteristics. (a) CW L-I curves from both facets of the device. (b) ASE spectra under a different current injection (Resolution: 0.1 nm). The inset shows the corresponding ASE ripples measured at 160 mA current (Resolution: 0.02 nm). (c) On-chip amplifier gain (blue) and on-chip output power (red) as a function of on-chip input power at 1290 nm wavelength. (d) On-chip gain (purple) and fibre-to-fibre NF (orange) as a function of wavelength with an on-chip input power of -28.5 dBm.

Figure 4(b) shows the ASE spectra measured from the output port (facet B) of the device from 20 to 200 mA with a step of 10 mA. The ASE spectra were obtained using the OSA (Yokogawa AQ6370D) with the resolution set to 0.1 nm. At low drive currents, the emission is dominated by the GS of the QDs centred at 1290 nm. At higher currents, the GS peak intensity saturates, and the sequential carrier filling of the QD's first ES1 centred at 1190 nm is subsequently observed. It has also been shown that with the increase of current, the GS peak wavelength initially decreases to 1287.36 nm at 60 mA originating from the state-filling effects of the QDs and then increases linearly at a rate of 0.057 nm/mA attributed to the device self-heating effect. A slower scan with the highest scanning resolution of the OSA (0.02 nm) was taken to analyze the ASE ripples at peak wavelength when the current is biased at 160 mA, as shown in the inset in Fig. 4(b). Even though achieving zero reflection from the facets is practically impossible, less than 0.03 dB power fluctuation implies excellent reflectivity suppression thanks to the tilted tapered waveguide and the high-quality AR coating.

A full depiction of the gain measurement of the SOA is presented in Fig. 4(c) and 4(d). The gain characteristics are independently verified with a commercial O-band tunable laser (Santec TSL-570). A programmable optical attenuator is connected subsequently to adjust the input power level. A polarisation controller (PC) is added at the input port of the SOA to modify the transverse-electric (TE) polarization state. Figure 4(c) examined the gain and saturation characteristics of the SOA by varying the input power at 1290 nm. As seen, the maximum on-chip gain in the linear regime is 24.5 dB when the current is biased at 160 mA, corresponding to a

high gain per length of 13.6 dB/mm. A further increase in current will shift the peak wavelength, so the optimum gain condition is no longer preserved at 1290 nm. The SOP of this device is 10 dBm at 160 mA, which is sufficient to integrate with the comb source developed in this work. Additionally, the SOP also experiences a slight increment as the current increases. The reason for that is the rate of band filling process of the carrier reservoir increases with the current pump density, so the GS can consume more carriers without reducing the gain [17]. Figure 4(d) displays the on-chip gain and fibre-to-fibre noise figure (NF) as a function of wavelength under different bias currents. The input power is -28.5 dBm which is well beyond the saturating point. It is evident that the gain bandwidth expands when the current increases from 100 mA to 200 mA. Concurrently, the peak of the gain spectrum is red-shifted, similar to the ASE spectra. The 3-dB gain bandwidth obtained from the graph is 21 nm at 160 mA, which is comparable to the corresponding ASE bandwidth (22.4 nm). Note that, strategies to improve the spectral bandwidth further are multifaceted: chirped QDs [10,40], QD intermixing [41], and hybrid QW/QD structures [42]. The overall NF between 1260-1320 nm is below 6.5 dB, with a minimum value of 5 dB obtained at 1290 nm.

3.3. Static characterisations of amplified ML-OFC

Figure 5(a) shows the comb lines of QD ML-OFC, ranging from 1287 nm to 1295 nm, before and after amplification by using QD SOA. The bias condition for QD ML-OFC and QD-SOA is 66 mA and 160 mA, respectively. As labelled in the graph, a total of 6 tones can be recognised within 3-dB bandwidth, with tone 3 located at 1290.55 nm being the highest. The peak output power is -6.05 dBm and tails off as the tones move away from the centre. The red line is the OSA trace of the amplified comb lines. The optical signal-to-noise ratio (OSNR) is decreased from 56.7 to 52 with amplification due to the noise contribution from ASE [17]. The output power of all channels is raised evenly after amplification, as 6 tones preserve within the 3-dB bandwidth. This consistency in the comb's spectral shape is attributed to the perfectly matched gain spectrum originating from the same QD wafer. The fibre-to-fibre gain for the individual tones from 1 to 6 is 4.47 dB, 4.31 dB, 4.18 dB, 4.29 dB, 4.13 dB, and 4.3 dB, respectively. It is worth pointing out that the gain of SOA is distributed into different comb lines, and the average gain for each tone is reduced with increasing the number of tones. Therefore, enhancing the optical gain of QD SOA is particularly crucial to meet the high power-per-channel demand for dense multi-channel amplification, especially with the QD active region, which in its nature, exhibits a lower confinement factor compared to its QW and bulk counterpart [43]. This peculiar carrier-photon interaction in QDs favours the SOP while reducing the modal gain [44]. There is still room for gain improvement through further optimization in QD material quality and structural design, such as increasing the cavity length and reducing the ridge waveguide width [17,45], as well as a sophisticated packaging scheme to minimise coupling loss.

The ability to maintain the pulse width after amplification is of significance for practical applications. Previously, an ultrafast and undistorted amplification of pulse trains from QD mode-locked lasers at 20, 40, and 80 GHz by a QD SOA at O-band was demonstrated, with the pulse broadening of 15% at 80 GHz [37,46]. Here, we investigate the pulse width broadening for the amplification of pulse trains with a record 100 GHz repetition rate. The pulse width was evaluated by an autocorrelator (the APE PulseCheck). As depicted in Fig. 5(b), according to the normalised Gaussian fitting curve, the pulse width of the comb source is 1.8 ps before amplification and is broadened by 14.4% after amplification. This pulse broadening effect at 100 GHz is smaller than what has been reported for amplifying an 80 GHz pulse train, attributed to the carefully optimized epitaxial growth, device design and fabrication.

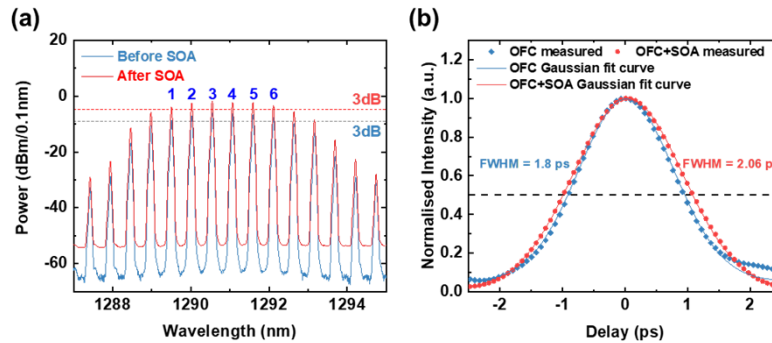


Fig. 5. Static characterizations of the amplified ML-OFC. Optical spectra from the OFC source of tones within 1287 nm-1295 nm before (blue line) and after amplification (red line). (c) Normalised autocorrelation trace with Gaussian pulse fitting of the OFC pulse before (blue line) and after amplification (red line).

3.4. Dynamic characterisations of amplified ML-OFC

Figure 6(a) and 6(b) summarise the RIN characteristics of the amplified comb lines, including the whole comb spectrum and three selected comb lines. The RIN spectrum was obtained from the noise measurement system ((SYCATUS A0010A) in the range of 100 MHz to 30 GHz. Noted that, three picked tones (tones 2, 4, 6) were filtered out by a tunable band pass filter (EXFO XTM-50) with each power level at ~ -14 dBm before being amplified. As shown in the inset of Fig. 6(b), the background noise level is suppressed to -70 dBm. The corresponding fibre-to-fibre gain of each isolated tone is 14.13 dB, 13.02 dB, and 14.46 dB, respectively. Considering the total coupling loss, the gain values are comparable to the measurement in the previous section. The fluctuation in the gain may result from variation in the polarization state since PC was adjusted for each independent measurement. Additionally, as the interplay between the charge carriers and input photons is not constant each time the current is injected, the beam profile may slightly shift in position. This beam instability creates uncertainty in coupling loss, given that the fibre was fixed in position. In the case of whole comb spectrum amplification, whose power level was at $+7$ dBm before amplification, the noise peak at 3.57 GHz represents the relaxation resonance frequency. The RIN value is maintained at around -160 dB/Hz for frequencies beyond 10 GHz. Interestingly, with the aid of QD SOA, the overall integrated average RIN value is reduced at low frequencies, with the peak level reduced to -153.5 dB/Hz. However, the noise level then exceeds the initial comb light at frequencies higher than 10 GHz. This phenomenon is further confirmed by examining isolated individual tones in Fig. 6(b). As seen, there was about a 10 dB difference in the high frequency RIN for cases with and without the SOA. It should be mentioned that the RIN is limited by high frequency noise since the lower limit of RIN is -157 dBc/Hz at an input power of 1 mW in this measurement system. As was expected, tone 6 exhibits a slightly higher modal RIN than the other tested tones, as it has the lowest output power since it is located farther from the peak wavelength than the other two. The RIN performance of filtered comb lines is reduced after amplification from 100 MHz to 5 GHz. Notably, this suppression in the modal RIN is no longer preserved at high frequencies, showing agreement with the whole spectrum amplification. The amplified noise performance for each tone is maintained at around -144 dB/Hz, whereas the modal RIN decreases significantly as frequency increases. Thus, at high frequencies (>5 GHz), the modal RIN contributed by the QD SOA is enlarged with the increased frequency. Even though the reduction in RIN with QD SOA from the input light has been discussed in many research works [47–49], the increase in modal RIN associated with QD SOA amplification at high frequencies has rarely been mentioned. Reducing the SOA's NF could

potentially remedy this issue. Nevertheless, this suppression in RIN at low frequencies renders QD SOA extra benefits in accelerating transmission rate with a low bit error rate (BER) in the fibre-optic communication [48].

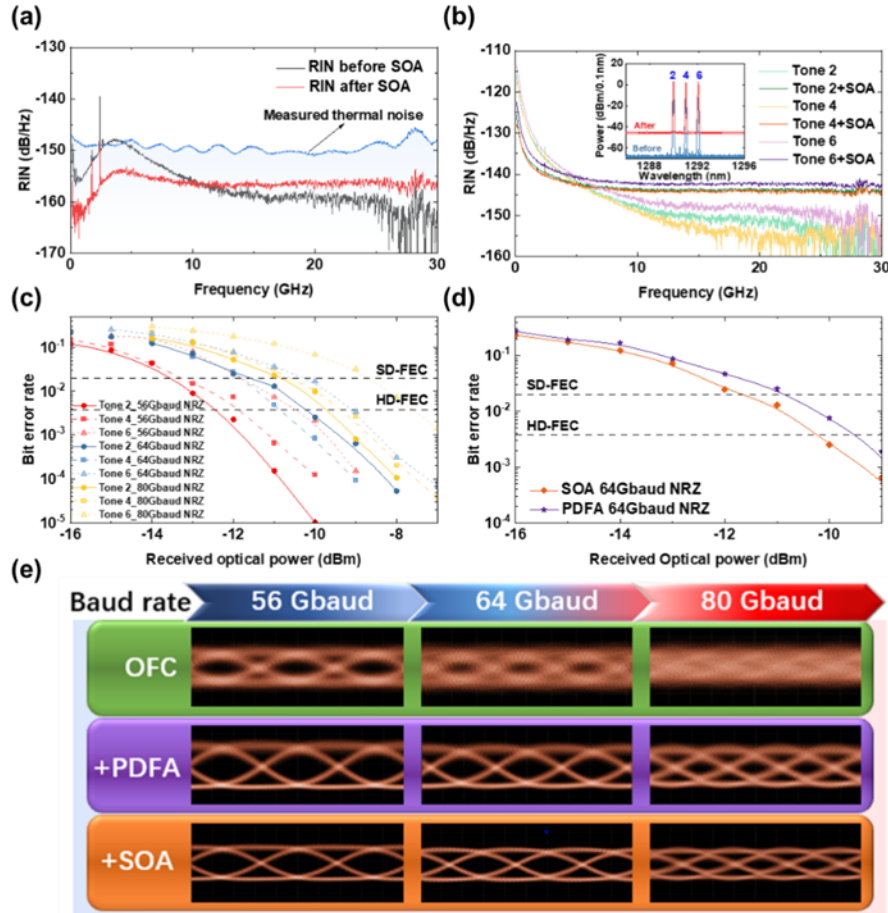


Fig. 6. Dynamic characterisations of the amplified ML-OFC. RIN spectra of (a) all comb lines and (b) filtered three tones within 3-dB bandwidth. (Inset: Optical spectra from the OFC source of filtered three tones within 3-dB bandwidth before (blue line) and after amplification (red line)). (c) 56 Gbaud, 64 Gbaud, and 80 Gbaud NRZ Back-to-back BER versus received optical power of the amplified filtered three tones. (d) 64 Gbaud NRZ back-to-back BER characteristics of the filtered tone 2 amplified by QD SOA and PDFA. (e) Optical eye diagrams for tone 2 before and after amplified by QD SOA and PDFA with 56 Gbaud, 64 Gbaud, and 80 Gbaud NRZ signal.

The practicality of high-speed data communication is then assessed by evaluating the BER performance of both devices at the system level. The transmission system setup is almost the same as the previous work [33], except that the PDFA before the Mach-Zander modulator is replaced by the QD SOA developed in this work. The pseudo-random binary sequence of an NRZ signal with a length of $2^{15}-1$ was generated to modulate the comb lines. The amplified comb light was then used as the optical carrier for fast transmission of up to 80 Gbaud NRZ signal. The back-to-back transmission BER versus the received optical power of the selected three tones is presented in Fig. 6(c). Unfortunately, the measurement of BER directly from the comb source is unattainable due to equipment limitations. Nonetheless, the closing optical eye diagrams

obtained from the comb source without amplification (as shown in Fig. 6(e)) also indicate an erroneous BER performance. Successful transmission of up to 80 Gbaud is demonstrated with the involvement of QD SOA in the system. As expected, the BER performance degrades with increasing baud rate, evidenced by the shift in BER curves towards higher received optical power. Not surprisingly, tone 6 presents the worst transmission performance owing to the high RIN level and low output power. The minimum received optical power is accomplished with tone 2. When the transmission rate is set to 56 Gbaud, the received optical power is -12.5 dBm for a BER of $3.8E-3$ (the hard decision forward-error-correction (HD-FEC) coding limit) and -13.6 dBm for a BER of $2E-2$ (the soft decision forward-error-correction (SD-FEC) coding limit), whereas the corresponding value for tone 6 is -9.8 dBm and -11 dBm, respectively. Figure 6(d) shows a direct comparison of tone 2 in 64 Gbaud BER transmission between QD SOA and the commercial optical pumped O-band PDFA (FiberLabs Inc. AMP-FL8611-OB-16) with the same amplification factor. The QD SOA outperformed the bulky, costly PDFA despite exhibiting a higher NF (NF measured by the PDFA at 1290 nm: 4.5 dB) and polarisation instability. The BER curve shows a quantified improvement of 0.8 dB received optical power in both SD-FEC and HD-FEC coding limits. As confirmed in Fig. 6(e), the QD SOA yields better optical eye diagrams with clear, symmetrical eye-opening, and distinct two levels up to 80 Gbaud. A previous study has presented the demonstration of BER measurement for QD SOA at 40 Gbaud under a repetition rate of 80 GHz [37], this work, to the best of our knowledge, marks the first-time error-free data transmission at 80 Gbaud under such a high repetition rate of ~ 100 GHz. Further advancements in chip packaging, such as utilising polarization maintaining fibre and fibre coupling scheme would deliver even more impressive performance. These high-speed transmission results indicate the high compatibility between ML-OFC and SOA, highlighting the importance of ultra-fast gain dynamics in QD.

4. Conclusion

We have developed a passively ML-OFC and SOA based on the same InAs/GaAs QD material. Owing to the unique advantages of ultra-fast carrier dynamics offered by the QDs, ultrafast and distortion-free amplification of QD ML-OFC with pulses down to a width of 1.8 ps at 100 GHz and up to 80 Gbaud/s non-return-to-zero (NRZ) data transmission with an SOA was achieved. By carefully deployment of these two key components with identical QD epi-structure, uniform power amplification for each comb line, less than 15% pulse shape broadening, and suppression in RIN level at the low-frequency region were demonstrated, deriving benefits from the perfect bandgap matching and ultra-fast gain recovery. Back-to-back transmission of up to 80 Gbaud/s NRZ data signal, together with the outperformed transmission results compared to the bulky, expensive commercial PDFA, suggest advanced QD echo system can be a promising DWDM solution offering direct electrical control, highly efficient operation, and monolithic integration opportunities.

Funding. Engineering and Physical Sciences Research Council (EP/T01394X/1, EP/T028475/1, EP/V02906/1).

Acknowledgments. The authors would like to acknowledge Mr. Jie Yan, Mr. Changqing Wang and Mr. Zhihang Liu from National Information Optoelectronics Innovation Center for device packaging. V.C. acknowledges the UK Engineering and Physical Sciences Research Council for funding her study.

Disclosures. The authors declare no conflicts of interest.

Data availability. Data underlying the results presented in this paper are not publicly available at this time but may be obtained from the authors upon reasonable request.

References

1. L. Chang, S. Liu, and J. E. Bowers, "Integrated optical frequency comb technologies," *Nat. Photonics* **16**(2), 95–108 (2022).
2. A. Hermans, K. Van Gasse, and B. Kuyken, "On-chip optical comb sources," *APL Photonics* **7**(10), 100901 (2022).

3. Y. Geng, H. Zhou, X. Han, W. Cui, Q. Zhang, B. Liu, G. Deng, Q. Zhou, and K. Qiu, "Coherent optical communications using coherence-cloned Kerr soliton microcombs," *Nat. Commun.* **13**(1), 1070 (2022).
4. A. Jørgensen, D. Kong, M. Henriksen, F. Klejs, Z. Ye, O. Helgason, H. Hansen, H. Hu, M. Yankov, and S. Forchhammer, "Petabit-per-second data transmission using a chip-scale microcomb ring resonator source," *Nat. Photonics* **16**(11), 798–802 (2022).
5. N. Picqué and T. W. Hänsch, "Frequency comb spectroscopy," *Nat. Photonics* **13**(3), 146–157 (2019).
6. I. Pupeza, C. Zhang, M. Högner, and J. Ye, "Extreme-ultraviolet frequency combs for precision metrology and attosecond science," *Nat. Photonics* **15**(3), 175–186 (2021).
7. J. Li, X. Yi, H. Lee, S. A. Diddams, and K. J. Vahala, "Electro-optical frequency division and stable microwave synthesis," *Science* **345**(6194), 309–313 (2014).
8. A. Baltuška, T. Udem, M. Uiberacker, M. Hentschel, E. Goulielmakis, C. Gohle, R. Holzwarth, V. S. Yakovlev, A. Scrinzi, and T. W. Hänsch, "Attosecond control of electronic processes by intense light fields," *Nature* **421**(6923), 611–615 (2003).
9. T. Steinmetz, T. Wilken, C. Araujo-Hauck, R. Holzwarth, T. W. Hansch, L. Pasquini, A. Manescau, S. D'odorico, M. T. Murphy, and T. Kentscher, "Laser frequency combs for astronomical observations," *Science* **321**(5894), 1335–1337 (2008).
10. S. Liu, X. Wu, D. Jung, J. C. Norman, M. Kennedy, H. K. Tsang, A. C. Gossard, and J. E. Bowers, "High-channel-count 20 GHz passively mode-locked quantum dot laser directly grown on Si with 4.1 Tbit/s transmission capacity," *Optica* **6**(2), 128–134 (2019).
11. J.-Z. Huang, Z.-T. Ji, J.-J. Chen, W.-Q. Wei, J.-L. Qin, Z.-H. Wang, Z.-Y. Li, T. Wang, X. Xiao, and J.-J. Zhang, "Ultra-broadband flat-top quantum dot comb lasers," *Photonics Res.* **10**(5), 1308–1316 (2022).
12. S. Pan, J. Huang, Z. Zhou, Z. Liu, L. Ponnampalam, Z. Liu, M. Tang, M.-C. Lo, Z. Cao, and K. Nishi, "Quantum dot mode-locked frequency comb with ultra-stable 25.5 GHz spacing between 20° C and 120° C," *Photonics Res.* **8**(12), 1937–1942 (2020).
13. W. Wei, J. Chen, J. Huang, Z. Wang, J. Zhang, and T. Wang, "Advances of semiconductor mode-locked laser for optical frequency comb generation," *Natl. Sci. Rev.* **1**(3), 20220026 (2022).
14. D. Liang, S. Srinivasan, G. Kurczveil, B. Tossoun, S. Cheung, Y. Yuan, A. Descos, Y. Hu, Z. Huang, and P. Sun, "An energy-efficient and bandwidth-scalable DWDM heterogeneous silicon photonics integration platform," *IEEE J. Sel. Top. Quantum Electron.* **28**(6), 1–19 (2022).
15. S. Cheung, Y. Yuan, Y. Peng, G. Kurczveil, S. Srinivasan, Y. Hu, A. Descos, D. Liang, and R. G. Beausoleil, "Demonstration of a 17× 25 Gb/s Heterogeneous III-V/Si DWDM Transmitter Based on (De-) Interleaved Quantum Dot Optical Frequency Combs," *J. Lightwave Technol.* **40**(19), 6435–6443 (2022).
16. S. Yamaoka, N.-P. Diamantopoulos, H. Nishi, R. Nakao, T. Fujii, K. Takeda, T. Hiraki, T. Tsurugaya, S. Kanazawa, and H. Tanobe, "Directly modulated membrane lasers with 108 GHz bandwidth on a high-thermal-conductivity silicon carbide substrate," *Nat. Photonics* **15**(1), 28–35 (2021).
17. T. W. Berg and J. Mork, "Saturation and noise properties of quantum-dot optical amplifiers," *IEEE J. Quantum Electron.* **40**(11), 1527–1539 (2004).
18. T. Akiyama, M. Sugawara, and Y. Arakawa, "Quantum-dot semiconductor optical amplifiers," *Proc. IEEE* **95**(9), 1757–1766 (2007).
19. S. Liu, J. Norman, M. Dumont, D. Jung, A. Torres, A. C. Gossard, J. E. Bowers, S. Liu, A. Torres, and A. Gossard, "High-performance O-band quantum-dot semiconductor optical amplifiers directly grown on a CMOS compatible silicon substrate," *ACS Photonics* **6**(10), 2523–2529 (2019).
20. A. Descos, G. Kurczveil, D. Liang, and R. Beausoleil, "Heterogeneous O-band InAs/GaAs quantum-dot optical amplifier on silicon," in *Asia Communications and Photonics Conference*, (Optical Society of America, 2021), paper W1F. 4.
21. D. Bimberg and U. W. Pohl, "Quantum dots: promises and accomplishments," *Mater. Today* **14**(9), 388–397 (2011).
22. F. P. García de Arquer, D. V. Talapin, V. I. Klimov, Y. Arakawa, M. Bayer, and E. H. Sargent, "Semiconductor quantum dots: Technological progress and future challenges," *Science* **373**(6555), eaaz8541 (2021).
23. T. Newell, D. Bossert, A. Stintz, B. Fuchs, K. Malloy, and L. Lester, "Gain and linewidth enhancement factor in InAs quantum-dot laser diodes," *IEEE Photonics Technol. Lett.* **11**(12), 1527–1529 (1999).
24. J. Duan, H. Huang, D. Jung, Z. Zhang, J. Norman, J. Bowers, and F. Grillot, "Semiconductor quantum dot lasers epitaxially grown on silicon with low linewidth enhancement factor," *Appl. Phys. Lett.* **112**(25), 251111 (2018).
25. T. Kageyama, K. Nishi, M. Yamaguchi, R. Mochida, Y. Maeda, K. Takemasa, Y. Tanaka, T. Yamamoto, M. Sugawara, and Y. Arakawa, "Extremely high temperature (220 C) continuous-wave operation of 1300-nm-range quantum-dot lasers," in *The European Conference on Lasers and Electro-Optics*, (Optica Publishing Group, 2011), paper PDA_1.
26. Y. Arakawa and H. Sakaki, "Multidimensional quantum well laser and temperature dependence of its threshold current," *Appl. Phys. Lett.* **40**(11), 939–941 (1982).
27. T. W. Berg and J. Mørk, "Quantum dot amplifiers with high output power and low noise," *Appl. Phys. Lett.* **82**(18), 3083–3085 (2003).
28. Y. Lu, X. Hu, M. Tang, V. Cao, J. Yan, D. Wu, J.-S. Park, H. Liu, X. Xiao, and S. Chen, "Analysis of the regimes of feedback effects in quantum dot laser," *J. Phys. D: Appl. Phys.* **55**(48), 484003 (2022).

29. Z. Liu, C. Hantschmann, M. Tang, Y. Lu, J.-S. Park, M. Liao, S. Pan, A. Sanchez, R. Beanland, and M. Martin, "Origin of defect tolerance in InAs/GaAs quantum dot lasers grown on silicon," *J. Lightwave Technol.* **38**(2), 240–248 (2020).
30. S. Chen, W. Li, J. Wu, Q. Jiang, M. Tang, S. Shutts, S. N. Elliott, A. Sobiesierski, A. J. Seeds, and I. Ross, "Electrically pumped continuous-wave III–V quantum dot lasers on silicon," *Nat. Photonics* **10**(5), 307–311 (2016).
31. Z.-H. Wang, W.-Q. Wei, Q. Feng, T. Wang, and J.-J. Zhang, "InAs/GaAs quantum dot single-section mode-locked lasers on Si (001) with optical self-injection feedback," *Opt. Express* **29**(2), 674–683 (2021).
32. J. C. Norman, D. Jung, Z. Zhang, Y. Wan, S. Liu, C. Shang, R. W. Herrick, W. W. Chow, A. C. Gossard, and J. E. Bowers, "A review of high-performance quantum dot lasers on silicon," *IEEE J. Quantum Electron.* **55**(2), 1–11 (2019).
33. S. Pan, H. Zhang, Z. Liu, M. Liao, M. Tang, D. Wu, X. Hu, J. Yan, L. Wang, and M. Guo, "Multi-wavelength 128 Gbit s⁻¹ λ-1 PAM4 optical transmission enabled by a 100 GHz quantum dot mode-locked optical frequency comb," *J. Phys. D: Appl. Phys.* **55**(14), 144001 (2022).
34. E. U. Rafailov, M. A. Cataluna, W. Sibbett, N. Il'Inskaya, Y. M. Zadiranov, A. Zhukov, V. Ustinov, D. A. Livshits, A. Kovsh, and N. Ledentsov, "High-power picosecond and femtosecond pulse generation from a two-section mode-locked quantum-dot laser," *Appl. Phys. Lett.* **87**(8), 081107 (2005).
35. M.-T. Choi, J.-M. Kim, W. Lee, and P. J. Delfyett, "Ultralow noise optical pulse generation in an actively mode-locked quantum-dot semiconductor laser," *Appl. Phys. Lett.* **88**(13), 131106 (2006).
36. E. Rafailov, P. Loza-Alvarez, W. Sibbett, G. Sokolovskii, D. Livshits, A. Zhukov, and V. Ustinov, "Amplification of femtosecond pulses over by 18 dB in a quantum-dot semiconductor optical amplifier," *IEEE Photonics Technol. Lett.* **15**(8), 1023–1025 (2003).
37. M. Laemmlin, G. Fiol, C. Meuer, M. Kuntz, F. Hopfer, A. Kovsh, N. Ledentsov, and D. Bimberg, "Distortion-free optical amplification of 20-80 GHz modelocked laser pulses at 1.3 μm using quantum dots," *Electron. Lett.* **42**(12), 697 (2006).
38. D. Bimberg, C. Meuer, G. Fiol, H. Schmeckebier, D. Arsenijevic, and G. Eisenstein, "Influence of P-doping in quantum dot semiconductor optical amplifiers at 1.3 μm," in *2009 11th International Conference on Transparent Optical Networks*, (IEEE, 2009), pp. 1–4.
39. T. W. Berg, J. Mörk, and J. M. Hvam, "Gain dynamics and saturation in semiconductor quantum dot amplifiers," *New J. Phys.* **6**, 178 (2004).
40. L. Li, M. Rossetti, A. Fiore, L. Occhi, and C. Velez, "Wide emission spectrum from superluminescent diodes with chirped quantum dot multilayers," *Electron. Lett.* **41**(1), 41–43 (2005).
41. K. Zhou, Q. Jiang, Z. Zhang, S. Chen, H. Liu, Z. Lu, K. Kennedy, S. Matchar, and R. Hogg, "Quantum dot selective area intermixing for broadband light sources," *Opt. Express* **20**(24), 26950–26957 (2012).
42. S. Chen, W. Li, Z. Zhang, D. Childs, K. Zhou, J. Orchard, K. Kennedy, M. Hugues, E. Clarke, and I. Ross, "GaAs-based superluminescent light-emitting diodes with 290-nm emission bandwidth by using hybrid quantum well/quantum dot structures," *Nanoscale Res. Lett.* **10**(1), 340 (2015).
43. C. Hantschmann, P. P. Vasil'ev, S. Chen, M. Liao, A. J. Seeds, H. Liu, R. V. Pentyl, and I. H. White, "Gain switching of monolithic 1.3 μm InAs/GaAs quantum dot lasers on silicon," *J. Lightwave Technol.* **36**(18), 3837–3842 (2018).
44. A. V. Uskov, T. W. Berg, and J. Mrk, "Theory of pulse-train amplification without patterning effects in quantum-dot semiconductor optical amplifiers," *IEEE J. Quantum Electron.* **40**(3), 306–320 (2004).
45. M. L. Davenport, S. Skendžić, N. Volet, J. C. Hulme, M. J. Heck, and J. E. Bowers, "Heterogeneous silicon/III–V semiconductor optical amplifiers," *IEEE J. Sel. Top. Quantum Electron.* **22**(6), 78–88 (2016).
46. C. Meuer, M. Laemmlin, G. Fiol, M. Kuntz, N. Ledentsov, A. Kovsh, S. Ferber, C. Schubert, A. Steffan, and A. Umbach, "High Frequency Signal Amplification using Quantum Dot Semiconductor Optical Amplifiers at 1.3 μm," in *2006 European Conference on Optical Communications*, (IEEE, 2009), pp. 1–2.
47. M. Yamada, N. Takeuchi, K. Sakumoto, and Y. Kuwamura, "Variation of relative intensity noise with optical power in InGaAsP semiconductor optical amplifier," *IEEE Photonics Technol. Lett.* **24**(22), 2049–2051 (2012).
48. D. Livshits, D. Yin, A. Gubenko, I. Krestnikov, S. Mikhrin, A. Kovsh, and G. Wojcik, "Cost-effective WDM optical interconnects enabled by quantum dot comb lasers," in *Optoelectronic Interconnects and Component Integration IX*, (SPIE, 2010), pp. 255–263.
49. M. Al-Qadi, M. O'Sullivan, C. Xie, and R. Hui, "On the Phase Noise Enhancement of a Continuous Wave in Saturated SOA Used for RIN Reduction," *IEEE Photonics Technol. Lett.* **32**(7), 430–433 (2020).